

## PHOTODISSOCIATION DYNAMICS OF $\text{Ar}_n^+$ CLUSTER IONS

TAKASHI NAGATA\*

*Department of Chemistry, Faculty of Science, The University of Tokyo,  
Bunkyo-ku, Tokyo 113, Japan*

*\*Department of Chemistry, College of Arts and Sciences, The University of  
Tokyo, Meguro-ku, Tokyo 153, Japan*

*(Received 23 March 1993)*

The time-of-flight (TOF) spectra of  $\text{Ar}^+$  and Ar fragments produced in the photodissociation of  $\text{Ar}_n^+$  ( $3 \leq n \leq 24$ ) were measured at wavelength around 540 nm. The kinetic-energy and angular distributions of the neutral photofragments were obtained for  $n = 3, 9$  and 24 by a simulation analysis of the measured TOF spectral profiles. The overall aspect of the photodissociation process of  $\text{Ar}_n^+$  is deduced from these distributions within the context of trimer ion core model; a linear  $\text{Ar}_3^+$  core is solvated by neutral Ar atoms. For  $\text{Ar}_n^+$  with  $4 \leq n \leq 14$ , direct dissociation of the  $\text{Ar}_3^+$  chromophoric core gives rise to  $\text{Ar}^+$  and/or Ar fragments with a high kinetic energy release. For the larger  $\text{Ar}_n^+$  ( $n \geq 14$ ), the production of high-kinetic-energy fragments is suppressed; “evaporation” of the solvent Ar atoms is instead the dominant channel of photofragmentation.

KEY WORDS: photofragment kinetic-energy and angular distributions

### 1. INTRODUCTION

The argon cluster ions,  $\text{Ar}_n^+$ , continue to receive much attention as a subject of theoretical<sup>1–11</sup> and experimental<sup>12–26</sup> studies in the field of cluster research. One of the fundamental issue regarding the  $\text{Ar}_n^+$  ions concerns the basic electronic structure of clusters; i.e., the extent of charge delocalization in the cluster ions. A marked difference in the electronic properties between  $\text{Ar}_2^+$  and  $\text{Ar}_3^+$  has been first revealed by Castleman and his coworkers,<sup>12</sup> and Lineberger and his coworkers.<sup>13</sup> They have found that  $\text{Ar}_3^+$  has a strong absorption band in the visible region around 520 nm, whereas the absorption band of  $\text{Ar}_2^+$  is located in the UV region near 300 nm.<sup>27,28</sup> Most of the theoretical calculations so far consistently predict a linear symmetric ( $D_{\infty h}$ ) conformation for  $\text{Ar}_3^+$  in the electronic ground state, where the positive charge is delocalized over three constituent atoms.<sup>2–8,10,11,19</sup> Figure 1 shows the potential energy curves for  $\text{Ar}_3^+$  obtained in the recent *ab initio* polarization configuration

interaction (POL-CI) calculations.<sup>11,19</sup> The visible absorption band of  $\text{Ar}_3^+$  is assigned to a  ${}^2\Sigma_g^+ \leftarrow {}^2\Sigma_u^+$  dissociative transition.

Levinger et al. have extended the photoabsorption measurements up to  $\text{Ar}_{40}^+$  and shown that the spectral features of the visible absorption band do not change with cluster size from  $n = 3$  until  $n = 15$ .<sup>14</sup> Those experimental results indicate that  $\text{Ar}_3^+$  remains as a chromophoric core in larger  $\text{Ar}_n^+$  ( $4 \leq n < 15$ ). Recent theoretical calculations using the diatomics-in-molecules (DIM) method<sup>5,10,11</sup> and Monte-Carlo calculations<sup>4</sup> also predict that the positive charge is concentrated on three Ar atoms in the cluster ions up to  $n \approx 14$ .

Alternative possibilities for the different substructure of  $\text{Ar}_n^+$  have also been proposed. Deluca and Johnson have discovered a UV absorption band in  $\text{Ar}_n^+$  ( $3 \leq n \leq 7$ ) near 300 nm,<sup>15</sup> which almost mimics the  ${}^2\Sigma_g^+ \leftarrow {}^2\Sigma_u^+$  band of  $\text{Ar}_2^+$ . Based on those findings, they have proposed a double minimum configuration for  $\text{Ar}_3^+$  such as  $\text{Ar}_2^+ \cdot \text{Ar}$ ; the UV band arises from an electronic excitation localized in the  $\text{Ar}_2^+$  moiety, and the visible band from an intracuster electron transfer excitation. The UV band structure has been confirmed by Magnera and Michl, who have determined the absolute photodissociation cross section of  $\text{Ar}_3^+$  over the 270–650 nm range.<sup>25</sup> The POL-CI results given in Figure 1 offer an alternative assignment for the UV band as the vibrationally-induced forbidden  ${}^2\Sigma_u^+ \leftarrow {}^2\Sigma_u^+$  transition.<sup>11,19</sup> Recently, Haberland et al. have re-examined the visible absorption band of  $\text{Ar}_n^+$  ( $3 \leq n \leq 80$ ) and found red-shift of the absorption maximum in the range  $n = 6$ – $9$ .<sup>21,22</sup> They have interpreted the spectral shift as a delocalization of the positive charge toward a tetramer core.

As shown in Figure 1, all the excited states of  $\text{Ar}_3^+$  except  ${}^2\Pi_g$  are strictly repulsive. Hence, photoabsorption inevitably leads to direct dissociation of  $\text{Ar}_3^+$  ion. The kinetic energy distribution of product  $\text{Ar}^+$  has been measured by several different groups at various wavelengths in the visible<sup>9,14–19</sup> and UV<sup>20</sup> regions. In all of those measurements, the product kinetic energy distribution shows strongly bimodal behavior; the distribution is composed of a high-kinetic-energy component near the energy conservation limit and a low-kinetic-energy component at almost zero kinetic energy. The bimodal kinetic energy distribution of the fragments is an obvious and unique “fingerprint” of the  $\text{Ar}_3^+$  photodissociation, which may be used to identify the core in larger  $\text{Ar}_n^+$ ; the photophysical properties of  $\text{Ar}_3^+$  is expected to remain in  $\text{Ar}_n^+$  involving a trimer core.<sup>23</sup> More recently, time-of-flight techniques have been applied to measure the kinetic energy distributions of neutral Ar fragments following the photoexcitation of larger  $\text{Ar}_n^+$  ( $4 \leq n \leq 25$ ).<sup>24,26</sup>

The present paper reports on the measurements of the photofragment time-of-flight (TOF) spectra of  $\text{Ar}_n^+$  ( $3 \leq n \leq 24$ ) in the visible region around 540 nm. Of particular interest is how the kinetic-energy and angular distributions of both ionic and neutral photofragments change with the size of cluster ions. The spectral profile of the measured TOF signal reflects the projection of the fragment velocity distribution along the detector axis. Therefore, analysis of the TOF spectra provides quantitative data on the kinetic-energy and angular distributions of the photofragments. Those

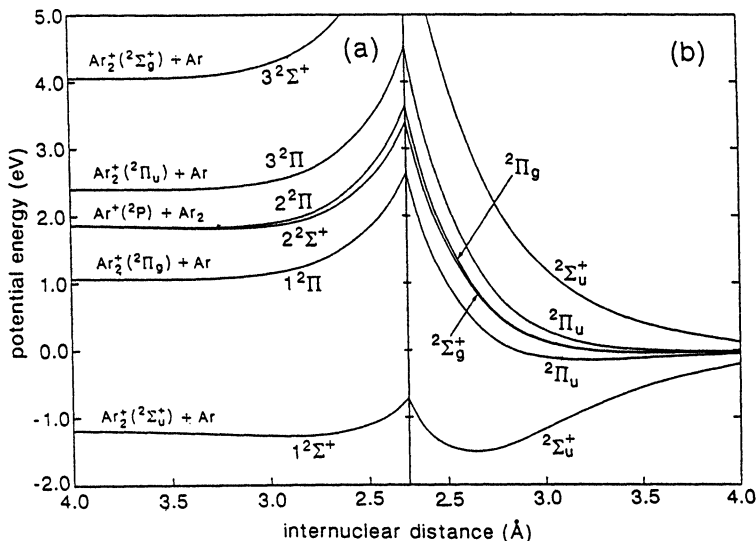


**Figure 1** *ab initio* POL-CI potential energy curves for  $\text{Ar}_3^+$  (taken from References 19). (a) The energy of a linear asymmetric  $\text{Ar}_3^+$  ( $C_{2v}$ ) as a function of internuclear distance between the separating atom and the middle one. The bond length of the remaining dimer (or dimer ion) is fixed to be 2.3 Å. Note that the  $2^2\Sigma^+$  and  $2^2\Pi$  states correlate to the  $\text{Ar}^+(2P) + \text{Ar}_2$  dissociation limit. (b) The energy of a linear symmetric  $\text{Ar}_3^+$  ( $D_{3h}$ ) as a function of internuclear separation between the middle and outer atoms. All the curves asymptotically approach the  $\text{Ar}^+(2P) + 2\text{Ar}$  dissociation limit.

experimental results are discussed in terms of the geometrical and electronic properties of  $\text{Ar}_n^+$ .

## 2. EXPERIMENTAL

Figure 2 depicts a schematic drawing of the experimental apparatus.<sup>26</sup> A beam of neutral argon clusters was produced by a pulsed free jet expansion of neat Ar gas through a 500  $\mu\text{m}$  orifice with a stagnation pressure of 4–5 atm. The  $\text{Ar}_n^+$  were produced by electron impact ( $\sim 20 \mu\text{A}$  at 200 eV) on the neutral cluster beam. The cluster ions were then extracted by applying a pulsed electric field and accelerated up to  $\sim 2$  keV. After traveling through a field-free flight path of  $\sim 83$  cm, the cluster ions were irradiated by either an output of a pulsed dye laser (Lambda Physik FL2002) pumped by a XeCl excimer laser (Lambda Physik EMG101) or the second harmonics (532nm) of a Nd:YAG laser (Quanta-Ray DCR-11) at the spatial focus of the ions. By varying the delay time between the pulse-extraction and the laser irradiation, the  $\text{Ar}_n^+$  parent ions were size-selectively photodissociated. Laser fluence was kept in the range  $\leq 10$  mJ/cm<sup>2</sup> for smaller  $\text{Ar}_n^+$  ( $n \leq 10$ ) and 2–4 mJ/cm<sup>2</sup> for larger  $\text{Ar}_n^+$  ( $n \geq 10$ ) in order to suppress multiphoton effects.<sup>26</sup> The direction of polarization vector,  $E$ , of the laser was set to be either parallel ( $\Theta = 0^\circ$ ) or perpen-

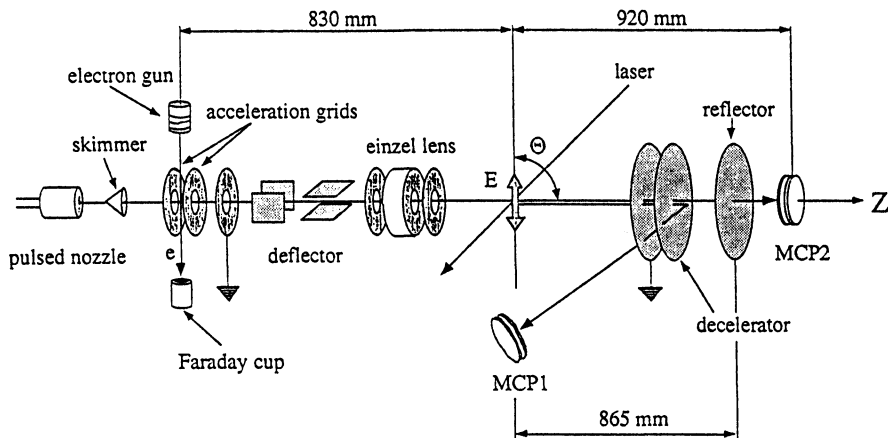


**Figure 2** Schematic diagram of the experimental apparatus. The angle between the laser polarization vector ( $E$ ) and the ion beam axis ( $Z$ ) is denoted by  $\Theta$ . The reflection angle of the ions ( $\sim 6^\circ$ ) is exaggerated in the figure.

dicular ( $\Theta = 90^\circ$ ) to the ion-beam axis (denoted as  $Z$  axis hereafter). Photofragment ions were successively mass-analyzed by a secondary reflectron mass spectrometer and detected by a microchannel plate (MCP1 in Figure 2). The retarding field of the reflectron was adjusted so as to reflect and focus only the fragment ions on the detector. The focusing condition was employed such that the ionic fragments having an identical mass but different kinetic energies reach the detector at different flight times. This enabled us to measure the kinetic energies of the fragment ions in the laboratory frame. Neutral fragments, which were not retarded by the reflectron, traveled along the  $Z$  axis and were detected by another microchannel plate (MCP2 in Figure 2) located behind the reflector. The time-of-flight data were accumulated typically for 400–800 shots, and then background signals due to collision-induced dissociation and/or metastable decay were accumulated with the photodissociation laser off. The photofragment TOF spectra were obtained by subtraction of the laser-off spectra from the laser-on spectra.

### 3. RESULTS AND DISCUSSION

#### 3.1. Photodissociation processes of $\text{Ar}_3^+$

Figure 3(a) shows the TOF spectra of  $\text{Ar}^+$  fragments following the photoexcitation of  $\text{Ar}_3^+$  at 555 nm. The spectra, shown as the upper and lower traces in Figure 3(a), respectively, were obtained with the  $E$  vector of the excitation laser parallel ( $\Theta = 0^\circ$ ) and perpendicular ( $\Theta = 90^\circ$ ) to the ion beam axis. The spectral profile obtained with  $\Theta = 0^\circ$  indicates a distinct bimodal kinetic energy distribution of the  $\text{Ar}^+$  fragments. The outer wings of the TOF peak are readily ascribed to high-kinetic-energy  $\text{Ar}^+$  fragments traveling into different scattering angles of  $0^\circ$  and  $180^\circ$  with respect

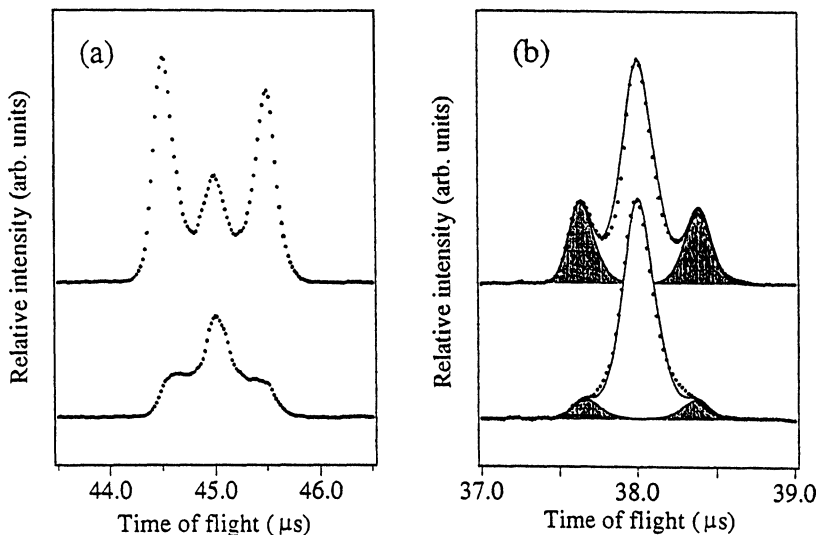
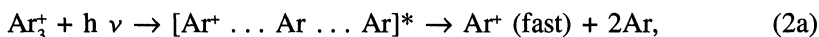


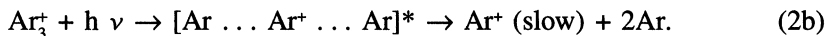
**Figure 3** Time-of-flight spectra of (a)  $\text{Ar}^+$  and (b)  $\text{Ar}$  photofragments from  $\text{Ar}_3^+$  recorded at 555 nm. The spectra were measured with the polarization vector  $E$  of the laser either parallel (upper trace) or perpendicular (lower trace) to the ion beam axis. The dots represent the experimental data. In panel (b), the simulated results are drawn by the solid lines. The calculated spectra are obtained by superposition of the contributions from  $P_s(\epsilon)$  and  $P_f(\epsilon)$ . The contribution from the fast component is shown by the shaded area.

to the direction of  $E$  vector. Hereafter, the high-kinetic-energy fragments will be referred as “fast” fragments. The center peak corresponds to  $\text{Ar}^+$  fragments which are almost stationary in the center-of-mass frame. These fragments will be denoted as “slow” fragments, hereafter. When the direction of  $E$  vector was rotated by  $90^\circ$ , the intensities of the outer wings were found to diminish significantly, while that of the center peak remains almost unchanged. The  $\Theta$  dependence of the spectral profile implies that the angular distribution of the fast  $\text{Ar}^+$  fragments is preferentially anisotropic along the  $E$  vector; in the  $\Theta = 0^\circ$  measurement the fragment ions having a sizable velocity component vertical to  $Z$  axis escape from the finite area of the detector. It is concluded from these observations that the fast  $\text{Ar}^+$  fragments, which give rise to the high-energy wings, are produced through a parallel-type transition; namely, the relevant transition dipole lies along the breaking bonds of  $\text{Ar}_3^+$ . The present results are quite consonant with the theoretical prediction that the  ${}^2\Sigma_g^+ \leftarrow {}^2\Sigma_u^+$  parallel-type transition is responsible for the photodissociation of  $\text{Ar}_3^+$ .<sup>11,19</sup>



where *direct* dissociation proceeds with the precursor  $[\text{Ar}_3^+]^*$  retaining a linear configuration. Within the context of this mechanism, the following two dissociation processes lead to the production of  $\text{Ar}^+$  fragments with different kinetic energy release:





In process (2a) one of the outer Ar atoms carries the positive charge during the dissociation and, as a result, a certain amount of energy near the energy conservation limit is partitioned to the translational motion of the product  $\text{Ar}^+$ . When process (2b) operates, the positive charge resides on the central Ar atom in the course of dissociation. Hence, the  $\text{Ar}^+$  fragment scarcely gains a translational energy under constraint of the momentum conservation.

When the photodissociation of  $\text{Ar}_3^+$  proceeds as processes (2a) and (2b), the *neutral* Ar fragments are also expected to have a bimodal energy distribution and an anisotropic angular distribution. One fast Ar and one slow Ar neutrals are formed through process (2a). Process (2b) may give two fast Ar neutrals. Figure 3(b) shows the TOF spectra of Ar neutrals from  $\text{Ar}_3^+$  at 555 nm. The intensities of the wings, which arise from high-kinetic-energy Ar neutrals, exhibit  $\Theta$  dependence almost identical with that observed in the  $\text{Ar}^+$  spectra. These observations, the spectral features of the Ar signal and their  $\Theta$  dependence, also support dissociation schemes (2a) and (2b).

As described above, a coarse examination of the TOF spectral features have provided a qualitative view of the kinetic-energy and angular distributions of the photofragments. More quantitative information on the distributions was obtained by a computer simulation of the TOF spectra. Details of the simulation method has been described previously.<sup>26</sup> Here, as an example, the simulated results are presented for the TOF spectra shown in Figure 3(b). In the simulation procedure, a Gaussian distribution was intuitively employed as a trial function for the kinetic energy distributions of the Ar fragments:

$$P_i(\epsilon_i) = C \exp \{(\epsilon - \epsilon^0)^2 / 2(\delta \epsilon_i)^2\}, \quad (i = s, f) \quad (3)$$

where the suffix  $i$  is for either the slow component (s) or the fast component (f),  $\epsilon^0$  corresponds to the kinetic energy at the distribution maximum,  $\delta \epsilon_i$  is the parameter determining the spread of the distribution, and C is a constant for normalization. The total kinetic energy distribution is expressed as a superposition of two Gaussian distributions:

$$P(\epsilon) = \alpha P_s(\epsilon) + (1 - \alpha) P_f(\epsilon), \quad (4)$$

where  $\alpha$  is the branching fraction for the slow Ar fragments. The photofragment angular distribution is given by<sup>29</sup>

$$I(\theta) = (1/4\pi) \{1 + \beta P_2(\cos \theta)\}, \quad (5)$$

where  $\theta$  represents the scattering angle of the particle with respect to the direction of E vector,  $\beta$  is an anisotropy parameter taking a value between  $-1$  and  $2$ , and  $P_2(\cos \theta)$  is the second degree Legendre polynomial. The  $\beta$  value for the slow component was fixed to be  $0$  in the simulation because the  $\Theta$  dependence, or rather its absence, of the TOF spectral features indicates an isotropic angular distribution for the slow Ar fragments. For the fast component,  $\beta$  was varied in the range from  $0$  to  $2$  in the simulation; the calculations with  $\beta \sim 1.5$  reproduced the observed results.

The calculated TOF distribution was convoluted with the energy distribution of the parent ions and the apparatus function prior to comparison with the observed TOF spectrum.

In Figure 3(b), the observed TOF spectra are compared with the simulated results. The calculated spectra reproduce the observed spectral profiles reasonably well in consideration of assuming rather simple trial functions of Equations (3) and (4). Figure 4(a) displays the kinetic energy distribution for reproducing the observed spectral profiles. The distribution clearly shows a bimodal behavior; one maximum is located at 0.02 eV and the other at 0.36 eV. The branching fraction,  $\alpha$ , is estimated

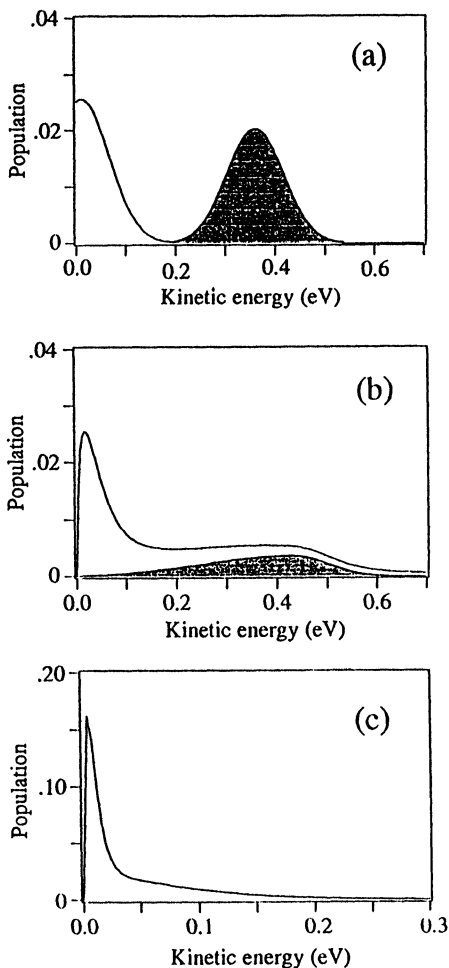


**Figure 4** Estimated kinetic energy distributions of the neutral Ar fragments in the center-of-mass frame. The parent cluster ions are (a)  $\text{Ar}_3^+$ , (b)  $\text{Ar}_9^+$  and (c)  $\text{Ar}_{24}^+$ , respectively. For  $n = 3$  and  $9$ , the distributions exhibit bimodal behavior. The shaded areas corresponds to the energy distributions of the fast components. Note the difference in the scales of panel (c).

to be  $\sim 0.42$  from the distribution function of Equation (4), indicating that the  $\text{Ar}_3^+$  photodissociation at 555 nm proceeds dominantly ( $\sim 85\%$ ) via process (2a).

### 3.2. Photodissociation processes of $\text{Ar}_4^+ - \text{Ar}_6^+$

When  $\text{Ar}_n^+$  ( $4 \leq n \leq 6$ ) is photolyzed in the wavelength range 470–580 nm,  $\text{Ar}^+$  and  $\text{Ar}_2^+$  are formed as primary products.<sup>23</sup> The photofragment TOF spectra for  $\text{Ar}_4^+$  measured at 540 nm are presented in Figure 5; the  $\text{Ar}_4^+$  spectrum is chosen here as a representative of  $4 \leq n \leq 6$ . For  $\Theta = 0^\circ$ , the spectrum consists of a ‘‘triplet’’ peak at the flight time  $\sim 57 \mu\text{s}$  and a ‘‘singlet’’ peak at  $\sim 61 \mu\text{s}$ . The former arises from  $\text{Ar}^+$  fragments and the latter from  $\text{Ar}_2^+$  fragments. In the measurement with  $\Theta = 90^\circ$ , the wings of the  $\text{Ar}^+$  peak reduce their intensities drastically, while the center peak almost retains its intensity. The ‘‘triplet’’ features and  $\Theta$ -dependence of the  $\text{Ar}^+$  peak are identical with those observed in the photodissociation of  $\text{Ar}_3^+$ ; i.e., the ‘‘fingerprint’’ of the  $\text{Ar}_3^+$  photodissociation. Therefore, it is rather straightforward to conclude that  $\text{Ar}_3^+$  is the chromophoric core of  $\text{Ar}_4^+$  and that  $\text{Ar}^+$  is produced directly via the dissociation of the trimer core:

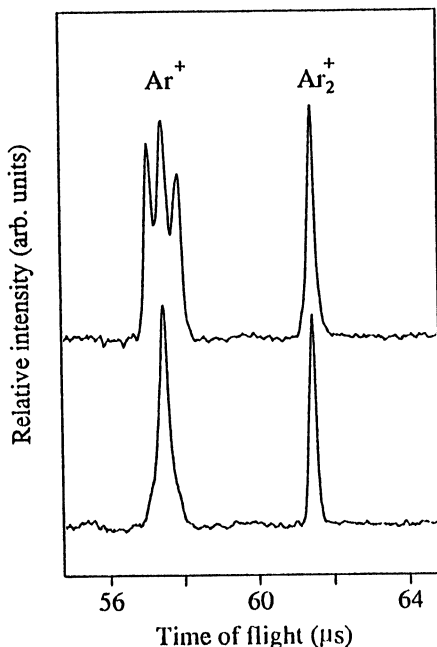
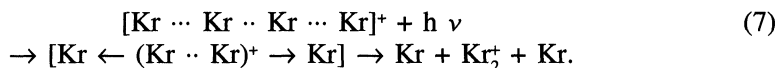


**Figure 5** Time-of-flight spectra of ionic photofragments from  $\text{Ar}_4^+$  measured at 540 nm. The polarization vector of the laser is either parallel (upper trace) or perpendicular (lower trace) to the ion-beam axis.

This conclusion is also supported by the fact that the  ${}^2\Sigma_g^+ \leftarrow {}^2\Sigma_u^+$  transition of  $\text{Ar}_3^+$  remains intact in the larger cluster ions with  $n < 15$ .<sup>14</sup> Recent DIM calculations predict that  $\text{Ar}_3^+$  core retains a linear geometry in  $\text{Ar}_n^+$  ( $4 \leq n \leq 25$ ); the trimer core is surrounded by Ar neutrals in such a way that both ends of the  $\text{Ar}_3^+$  axis remain “uncapped”.<sup>10,11</sup> Therefore, it is quite reasonable that the kinetic energy release along the  $\text{Ar}_3^+$  axis is preserved in the photodissociation of larger  $\text{Ar}_n^+$  ions.

While the spectral profile of the  $\text{Ar}_2^+$  signal scarcely changes with the angle of E vector, much closer examination has revealed that the  $\text{Ar}_2^+$  signal has broader tails in both sides of the peak for  $\Theta = 0^\circ$ . This implies that the  $\text{Ar}_2^+$  fragments carry a certain amount of kinetic energy and the fragment angular distribution is slightly anisotropic along the direction of E vector. Recently, Stace and his coworkers have measured the kinetic energy spectrum of  $\text{Ar}_2^+$  fragment produced in the photodissociation of  $\text{Ar}_4^+$  at 532 nm.<sup>24</sup> They found that the  $\text{Ar}_2^+$  fragments emerge with a low kinetic energy release and the profile of the energy spectrum displays *no* dependence on the angle of E vector. Chen et al. have also reported that the  $\text{Kr}_2^+$  fragment from  $\text{Kr}_4^+$  at ~600 nm photolysis has *zero* translational energy.<sup>30</sup> They have concluded that  $\text{Kr}_4^+$  has a linear structure which dissociates as



The present observation seems to be not all consistent with the earlier reports. In addition, the DIM results prefer a non-linear conformation for  $\text{Ar}_4^+$ ; the fourth Ar atom stays at the side of the linear  $\text{Ar}_3^+$  core.<sup>10,11</sup> In view of those discrepancies, there is an obvious need for further precise measurement of the kinetic energy distribution for the  $\text{Ar}_2^+$  fragments.

The intensities of the TOF signals were not directly proportional to the branching fraction for each fragment because not all the fragment ions were collected; high-kinetic-energy fragments having an off-axis velocity component escape from the acceptance angle of the detector. In order to estimate the branching ratio between  $\text{Ar}^+$  and  $\text{Ar}_2^+$  productions, the “escape efficiency” for a given fragment ion having a certain scattering angle and center-of-mass velocity was taken into account. After these corrections, the branching fraction for the  $\text{Ar}_2^+$  production from  $\text{Ar}_4^+$  was determined to be ~20% at 540 nm. The fraction was observed to increase as the photon energy decreases or the cluster size increases.<sup>19</sup> In other words, the dissociation channel which demands less energy is favored at a lower excitation energy and a larger cluster size. In the photodissociation of  $\text{Kr}_4^+$ , Chen et al. have observed an increasing tendency of the branching fraction of  $\text{Kr}_2^+$  fragments with increase of the photolysis wavelength.<sup>30</sup>

In spite of some discrepancies in the experimental results given by different groups, it seems still worthwhile to consider the mechanism of the  $\text{Ar}_2^+$  formation in terms of the potential energy surfaces of  $\text{Ar}_3^+$  because  $\text{Ar}_n^+$  ( $4 \leq n \leq 6$ ) absorbs a visible

photon through the  ${}^2\Sigma_g^+ \leftarrow {}^2\Sigma_u^+$  transition of the  $\text{Ar}_3^+$  core ion. The potential energy curves for  $\text{Ar}_3^+$  given by *ab initio* POL-CI calculations show that the  ${}^2\Sigma_g^+$  state correlates directly to the  $\text{Ar}^+$  ( ${}^2\text{P}$ ) +  $\text{Ar}_2$  dissociation limit but *not* to any of the  $\text{Ar}_2^+$  + Ar limits (see Figure 1). Within the framework of trimer ion core model, the  $\text{Ar}_2^+$  + Ar channel is accessible only through an internal conversion from the initially prepared  ${}^2\Sigma_g^+$  state to the lower electronic states,  ${}^2\Pi_u$  and  ${}^2\Sigma_u$ , which lead to the  $\text{Ar}_2^+({}^2\Sigma_u^+) + \text{Ar}$  and  $\text{Ar}_2^+({}^2\Pi_g) + \text{Ar}$  dissociation limits, respectively. The ‘‘solvent’’ Ar atoms behave as perturbers which may induce the internal conversion. The formation rate of the  $\text{Ar}_2^+$  fragments increases accordingly with the cluster size due possibly to increase of the effective number of perturbers.

### 3.3. Photodissociation processes of $\text{Ar}_7^+ - \text{Ar}_{12}^+$

In the photodissociation of  $\text{Ar}_n^+$  ( $7 \leq n \leq 12$ ) at 532 nm, the dominant fragment species is  $\text{Ar}_2^+$ :<sup>14,26</sup>



The available excess energy given by 532 nm photoabsorption is far above the threshold for breaking all the bonds of the neutral fragments into Ar atoms; the neutral fragments are likely to be produced as  $(n - 2)\text{Ar}$ . As a representative of cluster ions with size  $7 \leq n \leq 12$ , we choose here  $\text{Ar}_9^+$ . The argument described below is also applicable to  $\text{Ar}_n^+$  in the range  $n = 7-12$ .<sup>26</sup> The TOF spectrum of ionic fragments formed in the photodissociation of  $\text{Ar}_9^+$  at 532 nm displays a dominant peak of  $\text{Ar}_2^+$  (Figure 6(a)). The profile of the  $\text{Ar}_2^+$  peak does not change with the angle  $\Theta$ ; no indication was obtained for the production of any high-kinetic-energy fragment ions. By contrast, the TOF spectrum of the neutral fragments consists of a broad peak accompanied with small wings when the angle  $\Theta$  is set to be  $0^\circ$  (Figure 6(b)). These wings disappear almost completely in the measurements with  $\Theta = 90^\circ$ . It appears that neutral Ar atoms ejected with a high kinetic energy release give rise to the wings. The absence of  $\Theta$  dependence indicates that the central broad peak arises from Ar fragments having a low kinetic energy and an isotropic angular distribution.

The kinetic energy distribution of the neutral fragments was estimated by the computer simulation described above. The energy distribution of the slow Ar fragments was assumed primarily to obey a Boltzmann distribution because, as will be discussed below, the slow fragments possibly arises from ‘‘evaporation’’ processes. In the course of the simulation, it turned out that the observed spectral profile of the central broad peak was well reproduced by employing a superposition of two Boltzmann distributions with different effective temperatures.<sup>26</sup> For the energy distribution of the fast Ar fragments, an ‘‘asymmetric’’ Gaussian was employed:

$$P_f(\epsilon) = \begin{cases} C' \exp \left\{ (\epsilon - \epsilon_a^0)^2 / 2(\delta\epsilon_a)^2 \right\} & \text{for } \epsilon \leq \epsilon_a^0, \\ C' \exp \left\{ (\epsilon - \epsilon_b^0)^2 / 2(\delta\epsilon_b)^2 \right\} & \text{for } \epsilon \geq \epsilon_b^0. \end{cases} \quad (9)$$

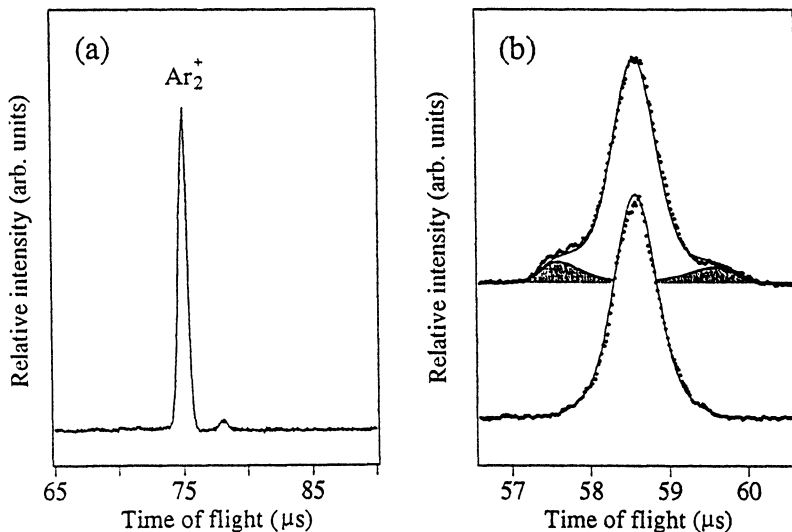
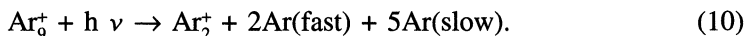


**Figure 6** Time-of-flight spectra of (a) ionic and (b) neutral photofragments from  $\text{Ar}_3^+$  measured at 532 nm. The TOF spectrum of the ionic photofragments shows no dependence on the angle  $\Theta$ . The spectra of the neutral photofragments were measured with the E vector either parallel (upper trace) or perpendicular (lower trace) to the ion beam axis. The dots represent the experimental data. The simulated results are drawn by the solid lines. The contribution from the fast component is shown by the shaded area. Note that the fast fragments scarcely make a contribution to the TOF signal for  $\Theta = 90^\circ$ .

The right-hand side of Equation (9) is readily reduced to a Gaussian if one sets  $\delta \epsilon_a = \delta \epsilon_b$ . Figure 4(b) displays the kinetic energy distribution which gives calculated spectra shown in Figure 6(b). The distribution has maxima at  $\sim 0.02$  eV and  $\sim 0.43$  eV. The branching fraction for the fast component is determined to be 0.29. Multiplying this value by the number of neutral Ar atoms formed in process (8), one obtains the average number of the fast Ar fragments;  $0.29 \cdot (9-2) = 2.03$ . It is now evident that the  $\text{Ar}_3^+$  photodissociation at 532 nm proceeds as



The results of the simulation analysis are summarized as follows: (1) the kinetic energy distribution of the neutral Ar fragments is bimodal; (2) two Ar neutrals are produced with a high kinetic energy release ( $\bar{\epsilon} \approx 0.35$  eV); (3) the  $\beta$  value was estimated to be in the range  $\sim 1.5$ – $2$  for the fast component; (3) the kinetic energy distribution of the slow Ar fragments obeys a “double” Boltzmann behavior with the effective translational temperatures of  $\sim 340$  K and  $\sim 2500$  K; (4) the angular distribution of the slow component is almost isotropic ( $\beta \sim 0$ ). Based on these findings, a possible dissociation mechanism is illustrated in Figure 7 within the context of trimer ion core model. The DIM calculations predict that the  $\text{Ar}_3^+$  core remains “uncapped” in  $\text{Ar}_3^+$  in the ground electronic state.<sup>6–8,19</sup> Upon photoabsorption, the trimer core starts to dissociate via the  $2^2\Sigma_g^+$  repulsive state. The two outer Ar atoms of the ion core separate along a symmetric stretching motion.<sup>6–8</sup> The

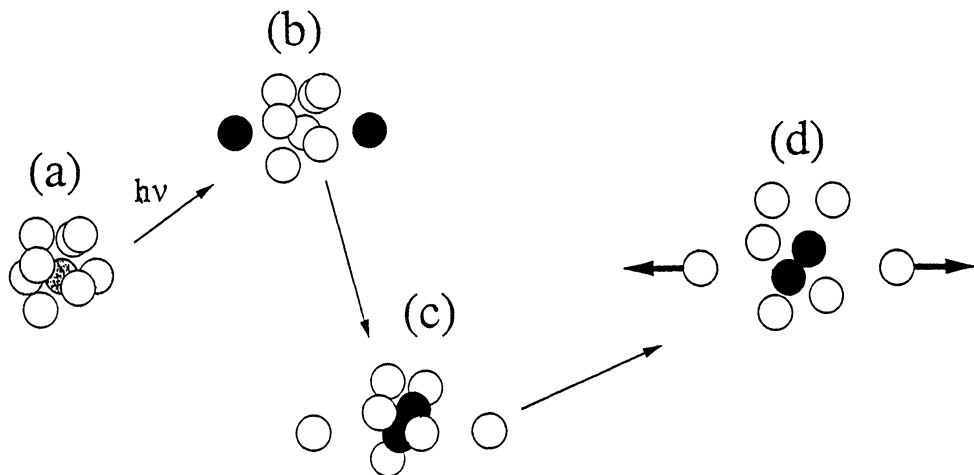


**Figure 7** Schematic of  $\text{Ar}_n^+$  photodissociation in the context of DIM structures. The initial geometry of  $\text{Ar}_n^+$  is obtained by the DIM calculations (References 10, 11). (a) The positive charge is concentrated on the three Ar atoms in the electronic ground state. The darkness of the shaded particles is roughly proportional to the charge concentration. (b) Upon photoexcitation, the positive charge tends to be localized on the recoiling outer atoms of the trimer core. (c) The charge transfer occurs from the separating atoms to form  $\text{Ar}_7^+$  cluster. The outer *two* atoms turn out to be fast neutral fragments. (d) The remaining “hot”  $\text{Ar}_7^+$  evaporates solvent atoms and, as a result, slow neutral fragments are formed. The dominant product ion is a vibrationally excited  $\text{Ar}_2^+$  having almost zero translational energy.

positive charge is localized on these recoiling Ar atoms as in the  $\text{Ar}_3^+$  photodissociation.<sup>6</sup> As the dissociation proceeds, the recoiling  $\text{Ar}^+$  transfers the charge back to form  $\text{Ar}_7^+$  because the charge delocalization in  $\text{Ar}_7^+$  resultingly stabilize the remaining system. Thus the system ejects *two* Ar neutrals with a high kinetic energy release and an anisotropic angular distribution. After the core dissociation, the  $\text{Ar}_7^+$  is likely to possess a fraction of the excess energy, which inevitably causes consecutive “evaporation” leading to the production of slow Ar atoms and an  $\text{Ar}_2^+$  ion. This model seems to be consistent with process (10), where *two* fast neutral atoms are formed. Thus, in  $\text{Ar}_n^+$  with  $7 \leq n \leq 12$ , the “fingerprint” of the  $\text{Ar}_3^+$  photodissociation remains in the kinetic-energy and angular distributions of neutral fragments but not in those of ionic fragments.

Recently, Haberland et al. have measured the photoabsorption spectra of  $\text{Ar}_n^+$  with  $3 \leq n \leq 80$  in the visible region and observed a gradual red-shift of the absorption maximum in the range  $n = 6-9$ .<sup>21,22</sup> They have argued that the observed spectral shift is ascribable to the core isomerization from a trimer toward a tetramer. In the present study, however, no indication was observed for the change in the photophysical properties in the range  $n = 7-12$ ; almost identical photodissociation mechanism involving a trimer ion core operates in  $\text{Ar}_{7-12}^+$ .

### 3.4. Photodissociation processes of $\text{Ar}_n^+$ with $n \geq 14$

Figure 8(a) shows the TOF profile for the ionic fragments produced in the photodissociation of  $\text{Ar}_{24}^+$  at 532 nm;  $\text{Ar}_{24}^+$  is the largest cluster ions studied in the present measurements. The product ions were found to be distributed over the range 2–11. The average size of the product ions was estimated to be 6. Thus, the photofragmentation proceeds, on average, as

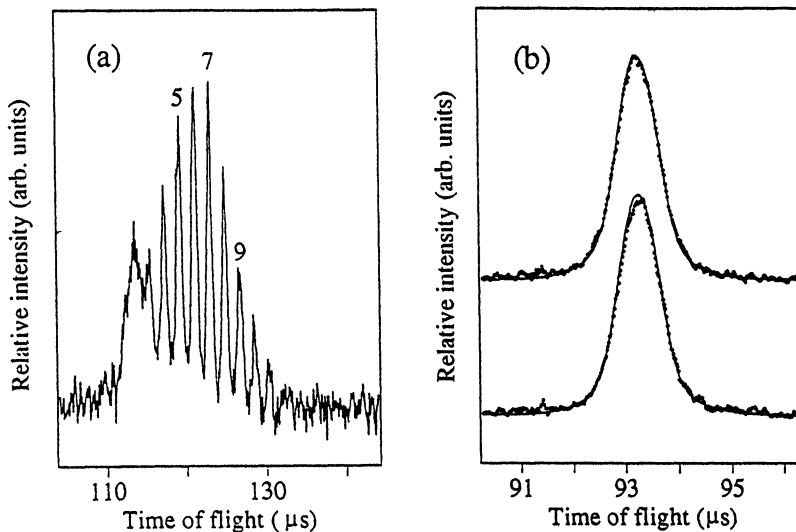


**Figure 8** Time-of-flight spectra of (a) ionic and (b) neutral photofragments from  $\text{Ar}_{24}^+$  measured at 532 nm. The spectra of both ionic and neutral fragments shows no dependence on the angle  $\Theta$ . The spectra of the neutral photofragments were measured with the E vector either parallel (upper trace) or perpendicular (lower trace) to the ion beam axis. The dots represent the experimental data. The simulated results are drawn by the solid lines.

In the TOF spectra of the neutral fragments, high-energy wings virtually disappear; the spectral features do not depend on the angle of E vector with respect to Z axis (Figure 8(b)). The absence of high-energy wings was observed also in the TOF spectra of the neutral fragments from  $\text{Ar}_n^+$  for  $n$  larger than 14. The simulation analysis of the TOF profile provided the kinetic energy distribution for the neutral fragments from  $\text{Ar}_{24}^+$ , as given in Figure 4(c). The kinetic-energy distribution is well represented by a “double” Boltzmann distribution with the effective temperatures of  $\sim 70$  K and  $\sim 600$  K. Thus, the distribution has no longer the high energy component characteristic of the direct dissociation of trimer core. The average translational energy of the

departing neutral atoms was calculated from the energy distribution;  $\bar{\epsilon} \approx 46$  meV. The  $\bar{\epsilon}$  value agrees surprisingly well with that given by Levinger et al.<sup>14</sup>; they gave an estimate of 45 meV for the kinetic energy of neutral atoms evaporating from  $\text{Ar}_n^+$  ( $n > 55$ ) on the basis of a statistical (RRK) model applied to the photofragmentation of  $(\text{CO}_2)_n^+$  clusters.<sup>31</sup> It is concluded from these considerations that the photodissociation of larger  $\text{Ar}_n^+$  ( $n \geq 14$ ) proceeds as an “evaporative” unimolecular decay of a vibrationally hot cluster ion. Following the photoabsorption, the energy available from a 532 nm photon is stored initially as an electronic energy of the chromophoric core. The energy is then dissipated swiftly through vibrational relaxation within the cluster. In consequence, the cluster ion is vibrationally heated leading to “evaporation” of the solvent atoms.

Very recently, Smith et al. have reported the presence of high-kinetic-energy neutral Ar atoms in the photodissociation of cluster ions up to  $\text{Ar}_{25}^+$ .<sup>24</sup> It seems possible that multiphoton process, which inevitably occurs under high fluence conditions of excitation laser, contributes to the production of fast neutrals in larger  $\text{Ar}_n^+$  with  $n \geq 14$ .<sup>26</sup>

A question regarding photodissociation dynamics of larger  $\text{Ar}_n^+$  still remains to be addressed; why the production of fast Ar neutrals is suppressed in the cluster ions larger than  $n \sim 14$ . The DIM calculations predict that  $\text{Ar}_n^+$  ( $14 \leq n \leq 19$ ) has an optimized geometry where one end of the  $\text{Ar}_3^+$  core is “capped” by solvent Ar atoms, while in  $\text{Ar}_n^+$  with  $n \leq 13$  both ends remain “uncapped”.<sup>10,11</sup> The calculations also predicts that, for the cluster ions up to  $\text{Ar}_{25}^+$ , the positive charge is localized on the trimer moiety in the electronic ground state, while the charge tends to spread over a larger moiety in the excited states. The extent of charge delocalization becomes significantly larger in  $\text{Ar}_n^+$  with  $n \geq 14$ , due possibly to an increasing interaction between the excited core and solvent atoms in the “capping” sites. It should be emphasized here that the “fingerprint” of the direct core dissociation, such as the production of high-kinetic-energy fragments and anisotropy in the fragment angular distribution, is smeared around the cluster size  $n \sim 14$ , as revealed in the present study.

### *Acknowledgements*

The author would like to thank Professor T. Kondow for helpful discussions, and Professor S. Iwata and Mr. T. Ikegami for valuable discussions on the theoretical calculations. Thanks are given to Messrs. J. Hirokawa, H. Okano and M. Sakamoto for their assistance in the experiment. A Mitsubishi 2000 1/s turbo molecular pump was supplied by courtesy of the Mitsubishi Heavy Industries Ltd. This research was supported by a Grant-in-Aid for Scientific Research from the Japanese Ministry of Education, Science and Culture.

*References*

1. H. H. Michels and R. H. Hobbs, and L. A. Wright. *Appl. Phys. Lett.*, **35**, 153 (1979).
2. W. R. Wadt. *Appl. Phys. Lett.*, **38**, 1030 (1981).
3. J. Hesslich and P. J. Kunz. *Z. Phys.*, D **2**, 251 (1986).
4. H. -U. Böhmer and S. D. Peyerimhoff. *Z. Phys.*, D **3**, 195 (1986); *Z. Phys.*, D **11**, 239 (1989).
5. P. J. Kunz and J. Valdorf. *Z. Phys.*, D **8**, 195 (1988).
6. F. X. Gadea and M. Amarouche. *Chem. Phys.*, **140**, 385 (1990).
7. F. X. Gadea. *Z. Phys.*, D **20**, 25 (1991).
8. F. X. Gadea and J. Durup. *Laser Chem.*, **11**, 95 (1991).
9. M. T. Bowers, W. E. Palke, K. Robins, C. Roehl, and S. Walsh. *Chem. Phys. Lett.*, **180**, 235 (1991).
10. T. Ikegami, T. Nagata, and T. Kondow. in *Physics and Chemistry of Finite Systems: From Clusters to Crystals*, edited by P. Jena, S. N. Khanna and B. K. Rao (Kluwer Academic, Dordrecht, 1992), Vol. I, p. 417.
11. T. Ikegami, T. Kondow and S. Iwata. *J. Chem. Phys.*, **98**, 3038 (1993).
12. C. R. Albertoni, R. Kuhn, H. W. Sarkas, and A. W. Castleman, Jr. *J. Chem. Phys.*, **87**, 5043 (1987).
13. N. E. Levinger, D. Ray, K. K. Murray, A. S. Mullin, C. P. Schulz, and W. C. Lineberger. *J. Chem. Phys.*, **89**, 71 (1988).
14. N. E. Levinger, D. Ray, M. L. Alexander, and W. C. Lineberger. *J. Chem. Phys.*, **89**, 5654 (1988).
15. M. J. Deluca and M. A. Johnson. *Chem. Phys. Lett.*, **162**, 445 (1989).
16. J. T. Snodgrass, C. M. Roehl and M. T. Bowers. *Chem. Phys. Lett.*, **159**, 10 (1989).
17. Z. Y. Chen, C. R. Albertoni, M. Hasegawa, R. Kuhn, and A. W. Castleman, Jr. *J. Chem. Phys.*, **91**, 4019 (1989).
18. C. A. Woodward, J. E. Upham, A. J. Stace, and J. N. Murrell. *J. Chem. Phys.*, **91**, 7612 (1989).
19. T. Nagata, J. Hirokawa, T. Ikegami, T. Kondow, and S. Iwata. *Chem. Phys. Lett.*, **171**, 433 (1990).
20. C. A. Woodward, B. J. Whitaker, and A. J. Stace. *J. Chem. Soc. Faraday Trans.*, **86**, 2069 (1990).
21. H. Haberland, T. Kolar, C. Ludewigt, A. Risch, and M. Schmidt. *Z. Phys.*, D **20**, 33 (1991).
22. H. Haberland, B. Issendorff, T. Kolar, H. Kormmeier, C. Ludewigt, and A. Risch. *Phys. Rev. Lett.*, **67**, 3290 (1991).
23. T. Nagata, J. Hirokawa, and T. Kondow. *Chem. Phys. Lett.*, **176**, 526 (1991).
24. J. A. Smith, N. G. Gotts, J. F. Winkel, R. Hallett, C. A. Woodward and A. J. Stace. *J. Chem. Phys.*, **97**, 397 (1992).
25. T. F. Magnera and J. Michl. *Chem. Phys. Lett.*, **192**, 99 (1992).
26. T. Nagata and T. Kondow. *J. Chem. Phys.*, **98**, 290 (1993).
27. J. T. Moseley, R. P. Saxon, B. A. Huber, P. C. Cosby, R. Abouaf and M. Tadjeddine. *J. Chem. Phys.*, **67**, 1659 (1977).
28. W. R. Wadt. *J. Chem. Phys.*, **73**, 3915 (1980).
29. R. N. Zare. *Mol. Photochem.*, **4**, 1 (1972).
30. Z. Y. Chen, C. D. Cogley, J. H. Hendricks, B. D. May and A. W. Castleman, Jr. *J. Chem. Phys.*, **93**, 3215 (1990).
31. P. C. Engelking. *J. Chem. Phys.*, **85**, 3103 (1986).